

A Chandra Legacy Observation of the LMC SNR N132D: Expansion of the Forward Shock

X. Long, P. P. Plucinsky, T.J. Gaetz & V. Kashyap on behalf of the N132D Legacy Team

Abstract

We present the first results from a deep (900 ks) observation of the Large Magellanic Cloud (LMC) supernova remnant N132D with the *Chandra X-ray Observatory*. N132D is an O-rich supernova remnant (SNR) of a 15-25 M_{\odot} progenitor and is the most X-ray luminous SNR in the Local Group ($L_{\text{X}} \sim 1.0 \times 10^{38}$ ergs s^{-1} [0.3-10.0 keV]). We compared the images of the bright rim in 2006 to our new data to derive an expansion of 0.097 ± 0.024 arcseconds over the 14.15 year baseline which corresponds to a **shock velocity of 1623 ± 402 km s^{-1} (0.0069 ± 0.0017 arcsecond yr^{-1}) for the southern rim**, and an **average shock velocity of 3843 ± 263 km s^{-1} for the north-east blowout regions**. Spectral fits to narrow regions near the shock front result in an **electron temperature of $T_{\text{e}} \sim 1.00$ keV for the southern regions**, and an **electron temperature $T_{\text{e}} \sim 0.77$ keV for the north-east regions** assuming a non-equilibrium ionization model with abundances typical of the interstellar medium in the LMC. This electron temperature of the southern regions implies a shock velocity of ~ 900 km/s assuming full electron-ion equilibration. The apparent discrepancy between the electron temperature inferred from the measured shock velocity and that inferred from the spectral fits may indicate that **the electrons and ions have not yet equilibrated in the southern forward shock region of N132D**. The electron temperature of north-east regions implies a shock velocity of ~ 800 km/s assuming full electron-ion equilibration. The discrepancy between the electron temperature inferred from the measured shock velocity and that inferred from the spectral fits would require a **cosmic ray acceleration efficiency of more than 50%**, which is **unlikely for these regions with spectra dominated by thermal emission**. It might indicate that we need **higher quality spectra and/or more complex models**.

N132D

N132D was classified as an O-rich remnant based on optical spectra (Lasker 1978). The remnant has a complicated morphology in X-rays (Fig. 1) with many bright filaments which appear along the line-of-sight to the interior of the remnant and several faint protrusions ahead of the brightest parts of the shock. The southwestern part of the remnant appears to have a semi-circular shell but the northeastern part of the remnant has a fragmented and decidedly non-spherical structure. A dense CO cloud has been mapped just to the south of the remnant (Banas et al. 1997, Sano et al. 2015). The X-ray, optical, and IR morphology are consistent with a remnant expanding into a cavity, and the bright shell emission indicates an interaction between the main blast wave and the cavity wall in the south (Hughes 1987 and Sharda et al. 2020). HST Faint Object Spectrograph (FOS) showed lines of C, O, Ne, & Mg but no evidence of Si, S, Ca, & Ar. Blair et al. (2000) suggested that the progenitor may have had an O-rich mantle which did not mix with the innermost ejecta layers. Early XMM results (Behar et al. 2001) show a centrally concentrated morphology in Fe-K emission, while O-K, Ne-K and Fe-L emission trace the outer bright parts of the shell. Vogt & Dopita (2011) constructed a 3D map of the [O III] filaments to show that the O ejecta form a ring 12 pc in diameter inclined ~ 25 degrees from the line of sight. Law et al. (2020) confirm a toroidal structure for the O ejecta, measuring velocities from -3000 to $+2300$ km s^{-1} and estimating an age of 2450 ± 195 yr. Borkowski et al. (2007) used the high-resolution image from *Chandra* to conclude that some of the O emission seen in X-rays (Fig. 2) is co-spatial with the O filaments seen in the optical. Bamba et al. (2018) analyzed *Suzaku* and *NuSTAR* data to conclude that the high energy emission could be explained by a $kT \sim 5$ keV equilibrium plasma or a $kT \sim 1.5$ keV recombining plasma. Hitomi et al. 2018 showed that the Fe-K emission is redshifted with a velocity of 800 km s^{-1} based on the first calorimeter spectrum. Sharda et al. 2020 used *Chandra* data to show that the Fe-K emission is located in the southern half of the remnant and estimated the progenitor mass to be $15 \pm 5 M_{\odot}$. Sano et al. 2020 found evidence of shock-heated CO clouds along the line of sight to the interior of the remnant.

Table 1: Archival Data and Cycle 20 Data

OBSID	Date	Exp(ks)	Used in Expansion	Roll Ang	Start FP Temp C	End FP Temp C
5532	2006-01-09	44.6	Y	329.9	-119.7	-119.7
7259	2006-01-10	24.9	Y	329.9	-119.7	-119.7
7266	2006-01-15	19.9	Y	329.9	-119.7	-119.5
21362	2019-03-27	34.9	Y	255.4	-110.7	-119.7
21363	2019-08-27	46.5	Y	105.0	-113.1	-119.7
21364	2019-09-01	21.0	Y	105.0	-111.6	-116.6
22687	2019-09-02	34.8	Y	102.5	-119.5	-119.7
22094	2019-09-10	36.6	Y	93.0	-119.2	-119.7
21687	2019-09-11	25.0	Y	93.0	-119.1	-119.7
22841	2019-09-12	36.9	Y	93.0	-113.7	-119.7
22853	2019-09-22	20.0	Y	93.1	-113.1	-116.8
22740	2019-09-26	20.0	Y	92.8	-111.6	-115.7
22858	2019-09-27	20.0	Y	92.7	-111.2	-116.0
22859	2019-09-28	19.0	Y	92.7	-111.5	-115.8
21881	2019-10-04	23.6	Y	84.5	-109.7	-115.8
22860	2019-10-06	18.0	Y	76.8	-112.5	-115.7
23270	2020-05-29	28.0	Y	178.1	-117.0	-119.7
21882	2020-05-30	35.0	Y	178.1	-112.9	-119.5
21883	2020-05-31	33.0	Y	178.1	-113.1	-119.5
23044	2020-06-02	53.5	Y	175.1	-111.5	-119.7
21886	2020-06-05	43.6	Y	175.1	-111.8	-119.7
21365	2020-06-07	57.0	Y	175.1	-113.4	-119.7
23277	2020-06-08	15.0	Y	183.1	-111.5	-114.4
21884	2020-06-09	43.0	Y	183.1	-116.3	-119.9
21887	2020-06-10	52.0	Y	183.1	-111.6	-119.7
21885	2020-06-25	21.6	Y	167.1	-111.8	-116.6
23286	2020-06-27	15.1	Y	167.1	-112.1	-114.4
21888	2020-07-11	25.1	Y	152.1	-115.7	-119.7
23303	2020-07-12	25.1	Y	152.1	-119.1	-119.7
21361	2020-07-13	31.5	Y	160.1	-112.4	-118.6

N132D Legacy Team

Aya Bamba (U. of Tokyo), William Blair (JHU), Daniel Castro (SAO), Adam Foster (SAO), Kristen Garofali (NASA/GSFC), Kosuke Hatauchi (U. of Tokyo), Charles Law (Harvard), Dan Milisavljevic (Purdue), Eric Miller (MIT Kavli Institute), Dan Patnaude (SAO), Hidetoshi Sano (NAOJ), Manami Sasaki (U. Erlangen-Nuremberg), Piyush Sharda (Australian National U.), Ben Williams (U. of Washington), Brian Williams (GSFC), Hiroya Yamaguchi (ISAS)

Observations and Registration

N132D was observed in 3 observations in 2006 and 28 observations in 2019 & 2020. Table 1 lists the observations and relevant details. Our analysis of the expansion of the forward shock relies on the measurement of small differences between the data in 2006 and 2019/2020. Therefore, we registered the images using point sources to improve the absolute astrometry provided by the default *Chandra* aspect reconstruction. The forward shock regions used in this analysis are shown in Figure 3, which displays the 2019/2020 data in the 0.35-8.0 keV band. Figure 4 shows which 9 point sources were selected for registration. Given that the roll angle and exposure time varied from observation to observation, the point sources that could be used for registration also varied from observation to observation. A minimum of 4 and a maximum of 7 point sources were used to register the observations to each other. We selected sources that were close to on-axis and sufficiently bright such that the **registration uncertainty is ~ 2 mas per source**. We selected the energy band of **1.2-7.0 keV** to minimize the impact on our analysis of the decreasing quantum efficiency (QE) of ACIS due to the buildup of the contamination layer. We selected 14 of the 28 observations amounting to a total of 582 ks of the total 878 ks to include in the expansion analysis in order to provide sufficient counts in the point sources for the registration.

Fig. 1: Extraction Regions (0.35-8.0 keV)

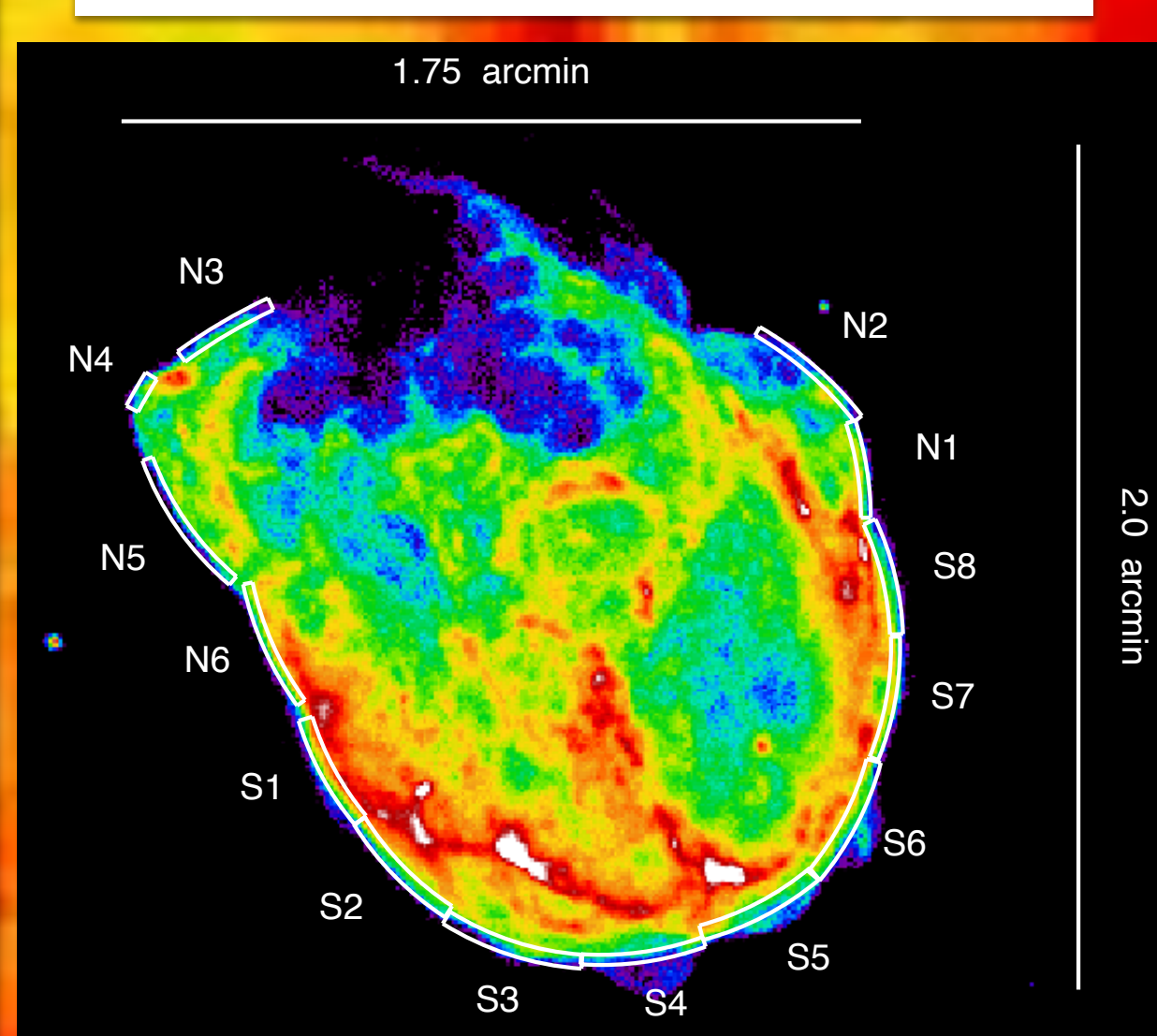
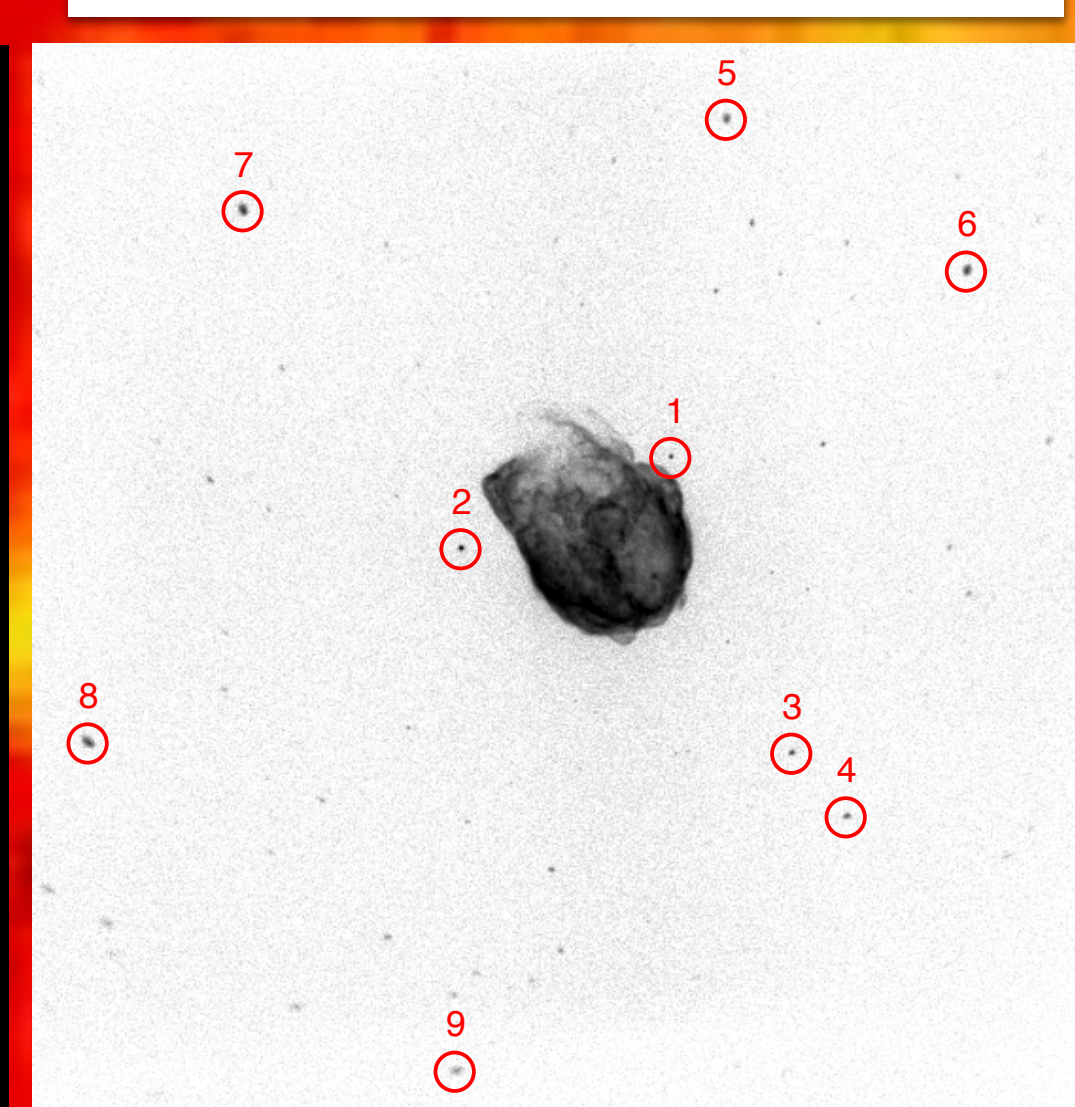


Fig. 2: Sources used for registration



Spectral Fits

We extracted spectra from the same regions used for the expansion analysis. We assumed a single component vps shock model modified by a Galactic absorption component fixed to 4.7×10^{20} cm^{-2} and variable absorption component (tbvarabs) with LMC abundances. The fit results are shown in Table 2 and representative fits for the southern region S3 (reduced $\chi^2 = 1.01/\text{DOF}=14634$) and north-east region N3 (reduced $\chi^2 = 1.12/\text{DOF}=14634$) are shown in Figures 4 & 5. The spectral plots show the 2006 data in red and the 2019/2020 data in black demonstrating the change in QE over time. The fitted abundances are consistent with LMC abundances and indicate that the emission in these regions is produced by swept-up interstellar material with little or no ejecta component. The fitted values of the temperature, kT_{e} , of the **southern ring vary from 0.76 keV to 1.20 keV with a mean of 0.97 keV**. This corresponds to a shock velocity of ~ 900 km/s assuming full equilibration between ions and electrons. Given that our measured shock velocity is approximately twice as large as this value, **it indicates that the ions and electrons are not in equilibrium**. The relatively low level of equilibration may be partially due to the fact that the progenitor exploded into a cavity created by its stellar winds and the shock has only recently encountered the dense material at the edge of the cavity. The fitted values of the **temperatures of north-east regions N3 & N4 are ~ 0.77 keV**, while the measured shock velocity implies a temperature of ~ 15 keV assuming full electron-ion equilibration. If we assume the electron temperature results from Coulomb collision with protons, **the inferred shock velocity implies that $> 60\%$ of the kinetic energy of the shock wave goes into cosmic ray acceleration**. Such a strong non-thermal component would result in synchrotron flux 100 times higher than is suggested by spectral fits that include power-law components, and implies a cosmic-ray acceleration efficiency much higher than the expected $\sim 10-20\%$. We posit that the cause of this discrepancy is that the ionization timescale is not reliably estimated from the spectral fitting.

Table 3. Shock region spectrum fit with a plane shock model. The best fitted parameter values with the 1σ uncertainties are listed.

Region	$N_{\text{H,LMC}}$	kT_{e}	τ	Norm	O	Ne	Mg	Si	S	Fe	C-stat	dof	χ^2_{p}
	10^{22}cm^{-2}	keV	$10^{11} \text{cm}^{-3} \text{s}$	10^{-4}									
S1	0.12	$0.98^{+0.02}_{-0.02}$	$1.48^{+0.10}_{-0.10}$	$6.16^{+0.24}_{-0.24}$	0.45	$0.52^{+0.03}_{-0.03}$	$0.36^{+0.02}_{-0.02}$	$0.49^{+0.03}_{-0.03}$	$0.52^{+0.06}_{-0.06}$	$0.37^{+0.02}_{-0.02}$	12824	14634	16541
S2	0.07	$1.20^{+0.04}_{-0.04}$	$1.39^{+0.10}_{-0.10}$	$1.97^{+0.24}_{-0.24}$	0.66	$0.51^{+0.06}_{-0.06}$	$0.47^{+0.05}_{-0.05}$	$0.61^{+0.05}_{-0.05}$	$0.40^{+0.07}_{-0.07}$	$0.51^{+0.05}_{-0.05}$	12174	14634	15116
S3	0.15	$1.14^{+0.04}_{-0.04}$	$0.88^{+0.09}_{-0.09}$	$1.44^{+0.10}_{-0.10}$	0.35	$0.40^{+0.05}_{-0.05}$	$0.45^{+0.04}_{-0.04}$	$0.55^{+0.06}_{-0.06}$	$0.59^{+0.12}_{-0.12}$	$0.51^{+0.09}_{-0.09}$	11787	14634	14846
S4	0.17	$1.01^{+0.10}_{-0.10}$	$1.54^{+0.39}_{-0.39}$	$0.80^{+0.11}_{-0.11}$	0.60	$0.39^{+0.09}_{-0.09}$	$0.51^{+0.08}_{-0.08}$	$0.49^{+0.08}_{-0.08}$	$0.66^{+0.17}_{-0.17}$	$0.53^{+0.09}_{-0.09}$	11397	14634	16912
S5	0.11	$0.94^{+0.04}_{-0.04}$	$1.36^{+0.11}_{-0.11}$	$2.12^{+0.11}_{-0.11}$	0.68	$0.45^{+0.05}_{-0.05}$	$0.52^{+0.05}_{-0.05}$	$0.61^{+0.06}_{-0.06}$	$0.72^{+0.12}_{-0.12}$	$0.62^{+0.06}_{-0.06}$	11945	14634	16125
S6	0.17	$0.76^{+0.02}_{-0.02}$	$1.09^{+0.12}_{-0.12}$	$3.43^{+0.19}_{-0.19}$	0.38	$0.54^{+0.03}_{-0.03}$	$0.45^{+0.03}_{-0.03}$	$0.50^{+0.04}_{-0.04}$	$0.65^{+0.13}_{-0.13}$	$0.38^{+0.03}_{-0.03}$	11777	14634	17797
S7	0.05	$0.79^{+0.02}_{-0.02}$	$2.23^{+0.20}_{-0.20}$	$2.04^{+0.12}_{-0.12}$	0.54	$0.64^{+0.05}_{-0.05}$	$0.63^{+0.05}_{-0.05}$	$0.62^{+0.06}_{-0.06}$	$0.47^{+0.10}_{-0.10}$	$0.49^{+0.05}_{-0.05}$	11276	14634	16108
S8	0.07	$0.91^{+0.03}_{-0.03}$	$0.98^{+0.12}_{-0.12}$	$1.18^{+0.09}_{-0.09}$	0.48	$0.60^{+0.06}_{-0.06}$	$0.46^{+0.05}_{-0.05}$	$0.58^{+0.07}_{-0.07}$	$0.46^{+0.12}_{-0.12}$	$0.49^{+0.02}_{-0.02}$	11221	14634	15690
N1	0.09	$0.81^{+0.05}_{-0.05}$	$1.14^{+0.19}_{-0.19}$	$1.20^{+0.11}_{-0.11}$	0.54	$0.64^{+0.06}_{-0.06}$	$0.49^{+0.06}_{-0.06}$	$0.57^{+0.08}_{-0.08}$	$0.64^{+0.12}_{-0.12}$	$0.40^{+0.05}_{-0.05}$	11078	14634	15195
N2	0.02	$0.94^{+0.06}_{-0.06}$	$0.61^{+0.10}_{-0.10}$	$0.60^{+0.05}_{-0.05}$	0.43	$0.78^{+0.07}_{-0.07}$	$0.50^{+0.07}_{-0.07}$	$0.65^{+0.11}_{-0.11}$	$0.84^{+0.29}_{-0.29}$	$0.33^{+0.05}_{-0.05}$	10853	14634	14053
N3	0.05	$0.77^{+0.05}_{-0.05}$	$1.37^{+0.24}_{-0.24}$	$1.25^{+0.11}_{-0.11}$	0.28	$0.40^{+0.04}_{-0.04}$	$0.28^{+0.05}_{-0.05}$	$0.44^{+0.08}_{-0.08}$	$0.50^{+0.18}_{-0.18}$	$0.35^{+0.05}_{-0.05}$	11220	14634	16410
N4	0.04	$0.77^{+0.05}_{-0.05}$	$1.15^{+0.21}_{-0.21}$	$0.83^{+0.10}_{-0.10}$	0.32	$0.52^{+0.05}_{-0.05}$	$0.26^{+0.04}_{-0.04}$	$0.31^{+0.07}_{-0.07}$	$0.52^{+0.20}_{-0.20}$	$0.28^{+0.04}_{-0.04}$	10661	14634	15380
N5	0.01	$0.72^{+0.03}_{-0.03}$	$1.03^{+0.12}_{-0.12}$	$1.14^{+0.09}_{-0.09}$	0.45	$0.67^{+0.05}_{-0.05}$	$0.46^{+0.05}_{-0.05}$	$0.53^{+0.08}_{-0.08}$	$1.31^{+0.27}_{-0.27}$	$0.49^{+0.05}_{-0.05}$	11045	14634	16523
N6	0.04	$0.74^{+0.03}_{-0.03}$	$1.65^{+0.18}_{-0.18}$	$3.28^{+0.20}_{-0.20}$	0.40	$0.55^{+0.03}_{-0.03}$	$0.51^{+0.04}_{-0.04}$	$0.53^{+0.04}_{-0.04}$	$0.66^{+0.14}_{-0.14}$	$0.49^{+0.05}_{-0.05}$	11609	14634	16017

Expansion Analysis

We extracted radial profiles from the registered 2006 and 2019/2020 data and searched for expansion. We assumed the 2019/2020 data as the "data" and the 2006 data as the "model". We shifted the model with respect to the data until the C statistic was minimized. The resulting shifts are plotted in Fig. 3 for the 14 regions. The red data points are from regions S1-S8 from the southern rim. The green data points are from regions N1-N6. The data points from the southern rim were fit with a constant (the blue line in Figure 3) to derive an expansion of 0.097 ± 0.024 arcseconds over 14.15 yr which corresponds to a velocity of 1623 ± 402 km/s. Note that regions N3 & N4 have a significantly larger expansion of ~ 0.230 arcseconds which corresponds to a velocity of $\sim 3843 \pm 263$ km/s. This would be consistent with the shock interacting with less dense material in the NE and suffering less deceleration than in the south.

Fig. 3: Expansion results for the 14 regions in Fig. 1

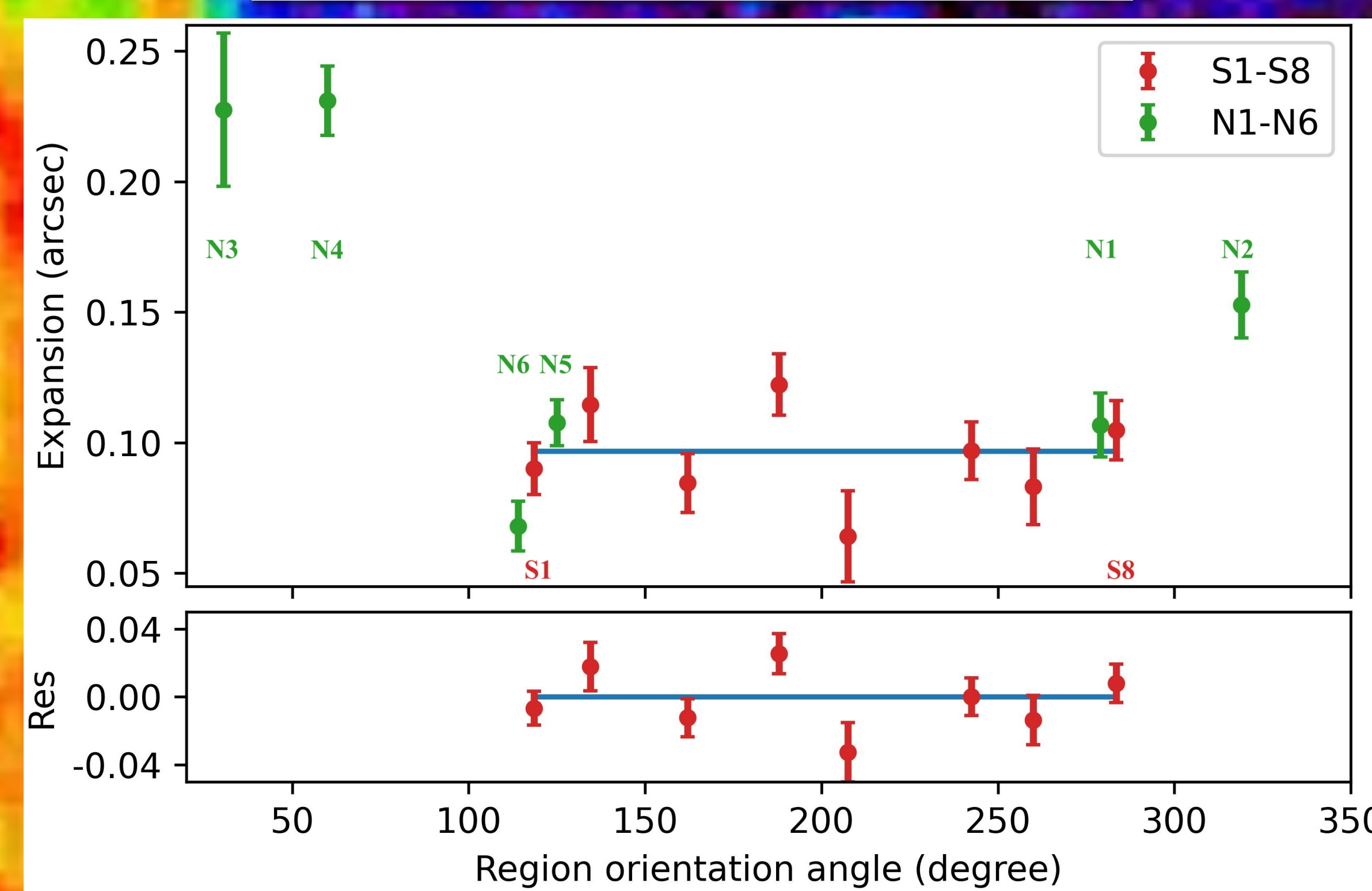


Fig. 4: Expansion velocities and the estimated expansion centers

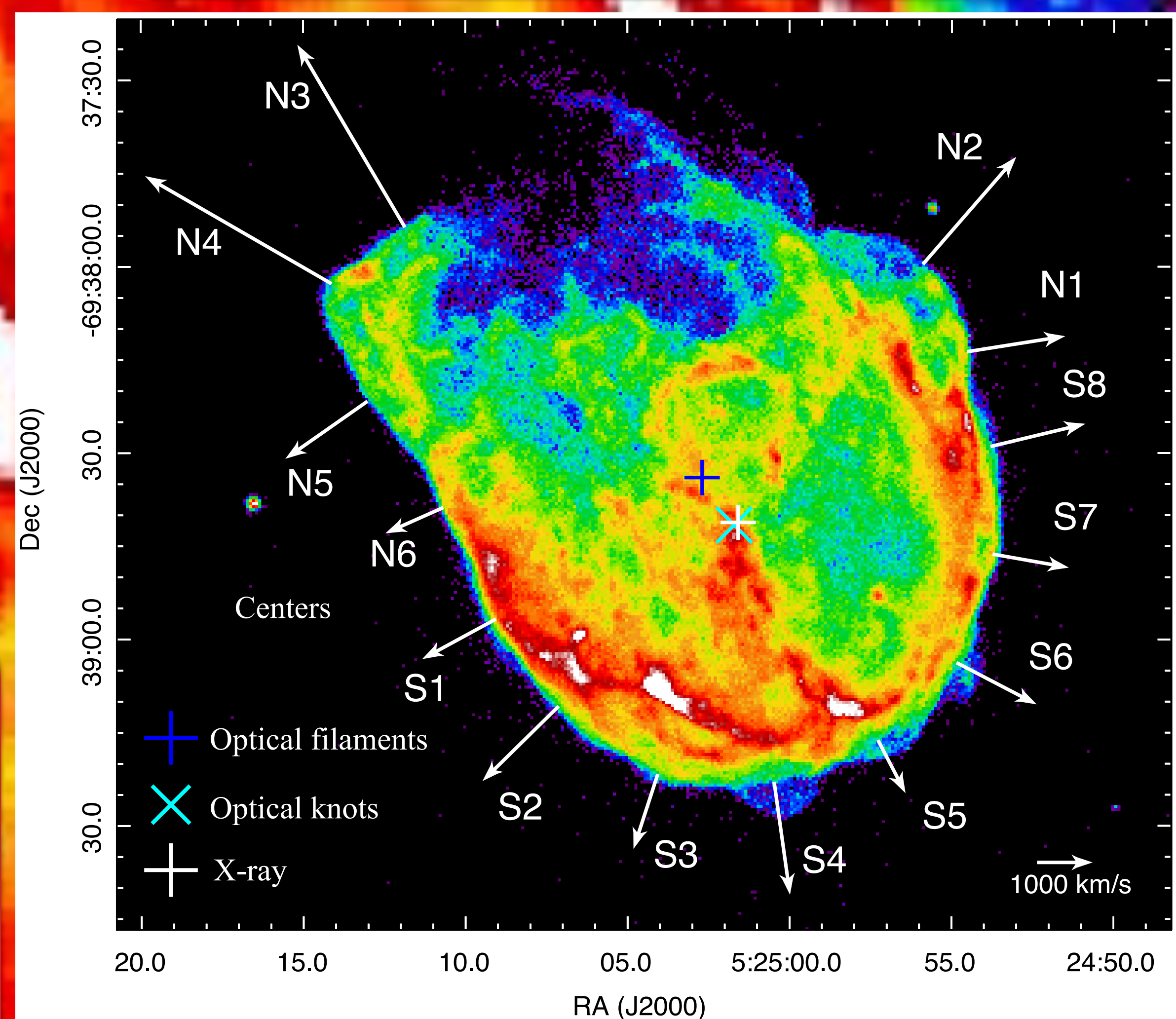


Table 2: Expansion centers in Fig. 4

Expansion centers	RA	DEC	
Morse et al. (1995)	05h 25m 02.70s	-69° 38' 34.00"	Optical filaments
Banovetz et al. (2023)	05h 25m 01.71s	-69° 38' 41.64"	Optical knots
estimated expansion center (based on regions S1-S8)	05h 25m 01.59s	-69° 38' 41.20"	X-ray

Fig. 5: Region S3 tbabs+tbvarabs+vpshock fit

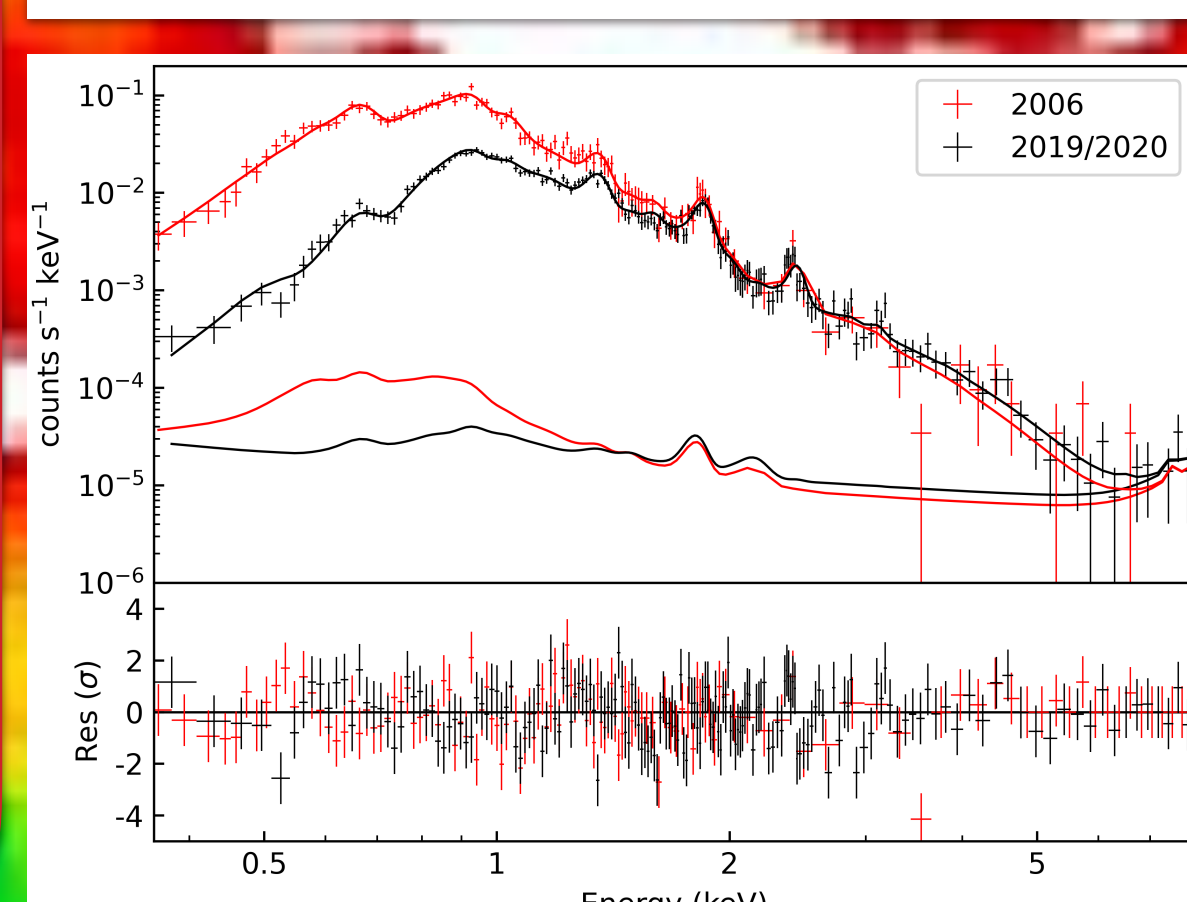
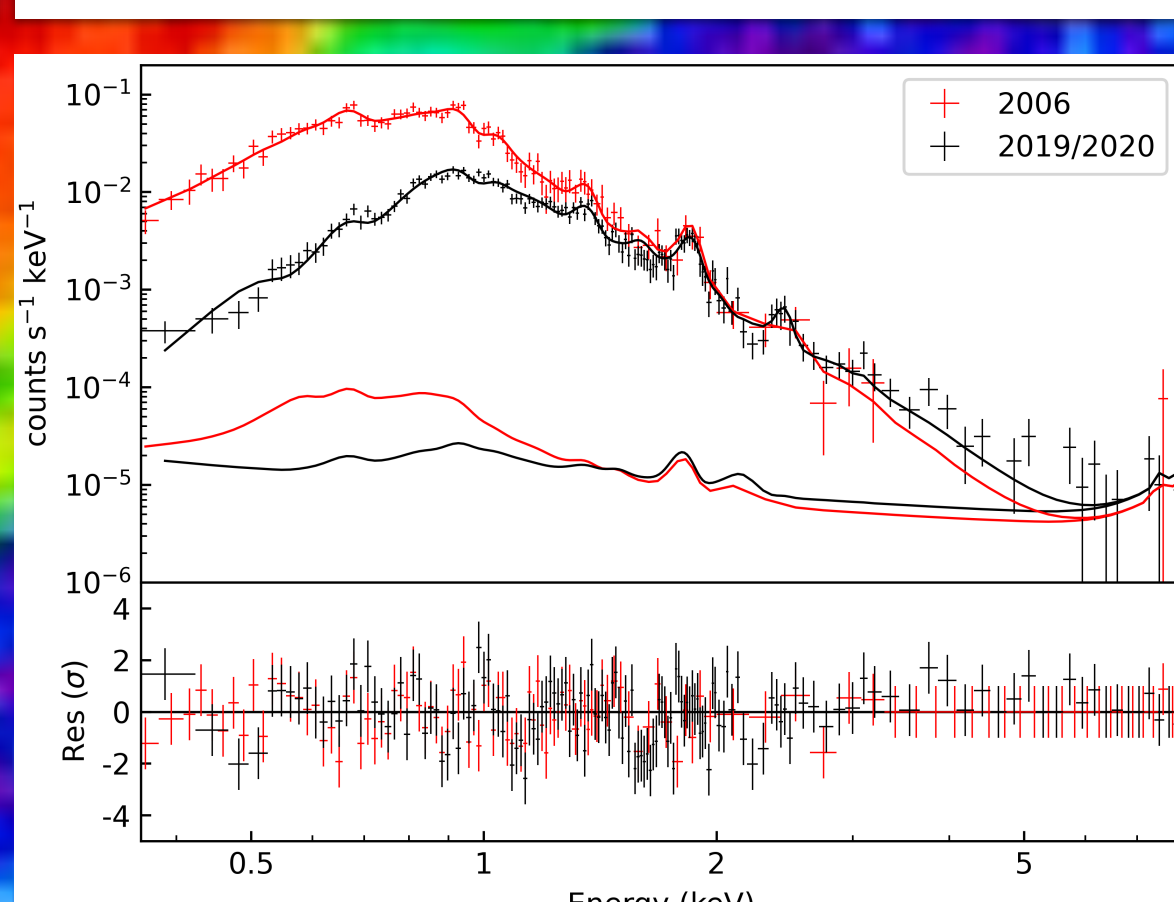


Fig. 6: Region N3 tbabs+tbvarabs+vpshock fit



References:

Banas, K.R. et al. 1997, ApJ, 480, 60
 Bamba, A. et al. 2018, ApJ, 854, 71
 Behar, E. et al. 2001, A&A, 365, L242
 Blair, W.P. et al. 2000, ApJ, 537, 667
 Borkowski, K.J. et al. 2019, ApJ, 671, L45
 Hitomi Collaboration, 2018, PASJ, 70, 16
 Hughes, J.P. 1987, ApJ, 314, 103
 J. C. Raymond, et al. arXiv:2303.08849
 Katsuda, S. et al. 2018, ApJ, 863, 127
 Lasker, B.M. 1978, ApJ, 223, 109
 Law, C.J. 2020, ApJ, 894, 73
 Sano, H. et al. 2015, ASP Conference Series, 499, 257
 Sano, H. et al. 2020, ApJ, 902, 53
 Sharda, P. et al. 2020, ApJ, 894, 175
 Sukhbold, T. 2016, ApJ, 821, 38
 Vogt, F., & Dopita, M.A. 2011, APSS, 331, 521